Functionally Graded Materials by Laser Metal Deposition

[1]Syamala R Pulugurtha, [1]Joseph Newkirk, [2]Frank Liou, and Hsin-Nan Chou[3]
[1]Department of Materials Science & Engineering, Missouri University of Science & Technology
[2]Department of Mechanical Engineering, Missouri University of Science & Technology
[3]Boeing Research & Technology

Abstract

Fabrication of functionally graded materials (FGMs) by laser metal deposition (LMD) has the potential to offer solutions to key engineering problems over the traditional metal-working techniques. But the issues that need to be addressed while building FGMs are intermixing in the layers and cracking due to the residual stresses. This paper is to present the study of the effect of process parameters (laser power and travel speed) on the degree of dilution between the substrate (or, previous layer) and powder material for few metallurgical systems.
Keywords: LMD, FGMs, intermixing, cracking, dilution

Introduction

FGMs for industrial-related applications have been a subject of research for quite some time now because of their ability to offer unique solution to the engineering problems over conventional materials and traditional composites. Among the various processing methods that are available, FGMs by LMD using solid free form fabrication route for obtaining bulk near net shape metallic components has been a promising technology. Its main advantage is the capability to control composition and properties within a fabricated structure by either pre-blending or combining different elemental powders using multiple powder feeder systems at the laser focal zone, which enables to tailor properties suited for specific engineering applications. This technology is ideal in producing functional prototypes and structural parts in smaller quantities and cost-effective [1,2,3].

Functionally grading dissimilar/incompatible metals (i.e. 100% A to 100% B) is qualitatively different from dissimilar/compatible systems [4] for the following reasons: (1) different thermo-physical properties, (2) composition becomes a parameter that can vary across the melt pool, and (3) nucleation of phases assumes importance, especially when inter-metallic compounds are present in the phase diagram. Although a lot of studies have been conducted on Ti-based systems by laser alloying, cladding, laser-rapid forming (LRF), etc. like Ti-N [5,6,7]; Ti-C-N [8], Ti-Al [9]; SiCp-Ti6Al4V [10]; TiC-Ti6Al4V and TiC+NiCrBSi –Ti6Al4V [11]; Ti-xV, Ti-xMo [12], a very limited literature is available on Ti based alloy/Ni FGMs [13], or Ti based alloy/ Fe FGMs. The dissimilar systems such as Ni-Ti have following features: (a) different thermo-physical properties, for example, thermal diffusivity of Ni is roughly three times that of Ti at room temperature and density of liquid Ni is twice that of liquid Ti, and this significantly influences heat transfer. (b) There are three inter-metallic phases (IMPs) in the system which can form from the liquid through invariant reactions. Lin *et al* [13] successfully deposited a FGM having a continuous gradient from 100% Ti to 60% Rene88DT superalloy by LRF. They investigated the phase evolution during solidification and attributed the hardness of the graded material to be dependent on the amount and morphology of the phases: Ti_2Ni, TiNi, and $\alpha + Ti_2Ni$ eutectoid. Most of the previous studies were focused on understanding the solidification behavior and phase evolution in multi-component systems, but the issues like intermixing in the layers, cracking due to thermal and residual stresses have not been dealt with. With this in mind, the present work focuses on the effect of process parameters like laser power

and travel speed on intermixing in the layers, and the pre-treatment (i.e. substrate heating) of the substrate to try counter cracking issues.

Experimental

Our LAMP system (Fig. 1(a)) consists of a 1 kW diode laser (Nuvonyx ISL-1000M, 808 nm, spot size 2.5 mm), a five-axis numerical control working table, and a powder feeder with co-axial nozzle was used to fabricate the graded materials. The experiments were conducted in an argon-gas environment to prevent the melt pool from oxidizing and oxide contamination from occurring during processing. The powder stream from the hopper was directly injected using argon gas into the molten pool through the laser nozzle. The metal powder was melted and subsequently re-solidified to form the clad layer (Fig. 1(b)). The typical size of the powders was in the range of 100-45 microns. The nominal composition of Fe-82 wt% V (powder-1) and Inconel-625 (powder-2) powders are listed in Table 1. The substrate materials used for the experiment were cold rolled 1 in. thick Ti6Al4V and SS316L. The substrates were cleaned prior to deposition using ethyl alcohol to remove any dirt or grease on the surface.

Table 1: The chemical composition (wt%) of the powders

Type of Powder	***Composition (wt%)***
Powder-1: Fe-82 wt% V	V (82), Al (0.68), Si (0.9), C (0.07), S (0.01), P (0.02), Fe (18)
Powder-2: Inconel-625	Ni (58), Cr (20-23), Mo (8-10), Nb+Ta (3.15-4.15), Fe (5)

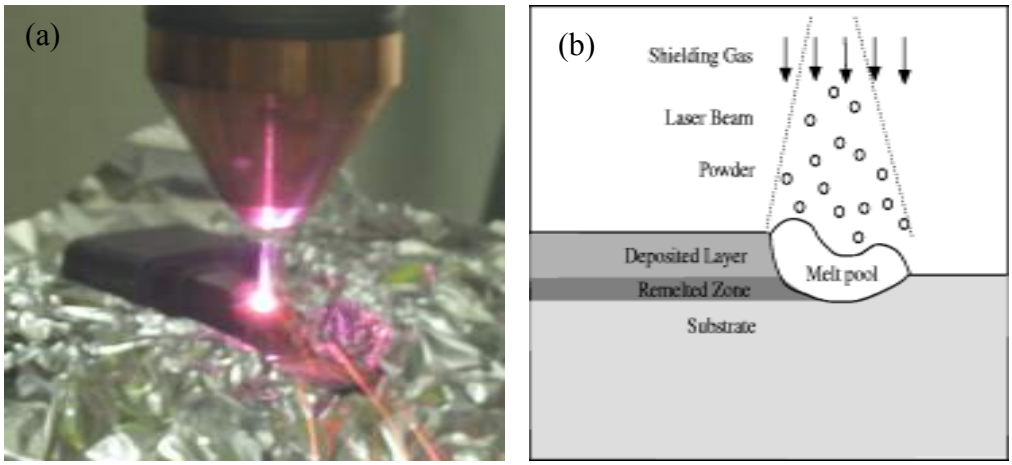

Fig. 1: (a) LAMP system (fig. shows repair welding); (b) Schematic of the deposition process.
(Source: http://www.emeraldinsight.com/fig/1560130405005.png)

The as-deposited material was sectioned parallel to the compositional gradient for microscopy studies; for X-ray diffraction (XRD) analysis, the perpendicular section was utilized. The composition along the gradient direction was characterized using scanning electron microscopy (SEM): Hitachi S570 equipped with a Si-drift energy dispersive X-ray (EDS) analysis facility. The identification of phases was achieved using X-Ray Diffraction (XRD)

(Philips Xpert X-ray diffractometer), and micro-hardness of the deposits was measured using Struers (model: Duramin).

Results and Discussion

Composition and Phase Analysis

In order to understand the effect of residual heat on inter-mixing/cracking with change of laser power on each deposited layer, a simpler experiment was designed by changing the power (Ramp up & Down) every 0.9th inch on a single layer track; parameters listed in Table 2. In case of powder-1, cracks were observed on both the substrates for all the processing parameters. The Fe-V equilibrium phase diagram (Fig. 2(a)) shows σ-phase is more likely to form in austenitic steels when there is ferrite retained from high temperature operation. Also, V is a ferrite stabilizer and forms brittle σ-phase (needle like structure) under processing conditions. XRD phase analysis results further corroborates the presence of only BCC-Fe 2θ peaks in powder-1 deposit on SS316L, as shown in Fig. 3. The combination of brittle phases and residual stresses probably may have caused cracking in the powder-1 deposit on SS316L for all the processing parameters.

Table 2: Processing parameters for different power profiles,
* Ti6Al4V and SS316L substrates, powder-1 & 2

Exp. Type	Power, W	Trvl. Spd., ipm	Pwd. Feed Rt., g/min
Ramp-Up	300, 387.5, 475, 562.5, 650, 737.5, 825, 912.5, 1000	10	5
Ramp-Down	1000, 912.5, 825, 737.5,650, 562.5,475,387.5,300		

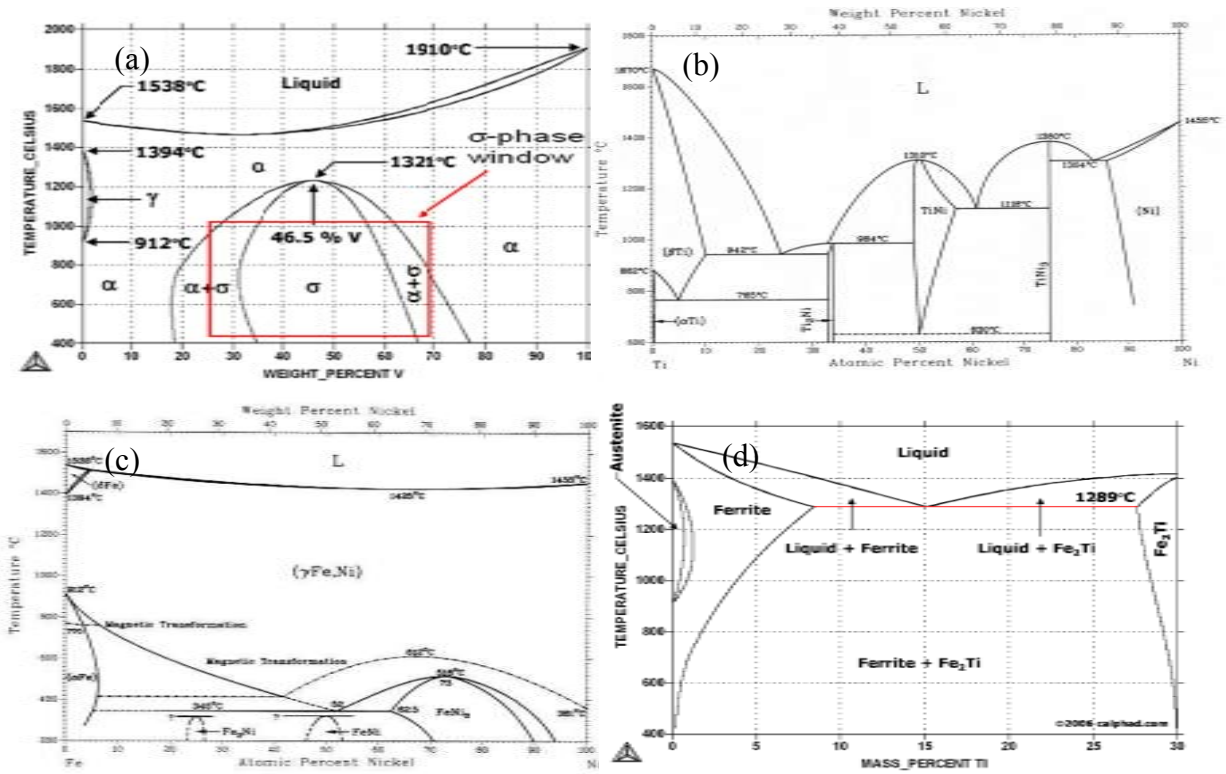

Fig. 2: Equilibrium phase diagrams: (a) Fe-V; (b) Ni-Ti; (c) Fe-Ni; (d) Fe-Ti (Source: www.calphad.com/graphs)

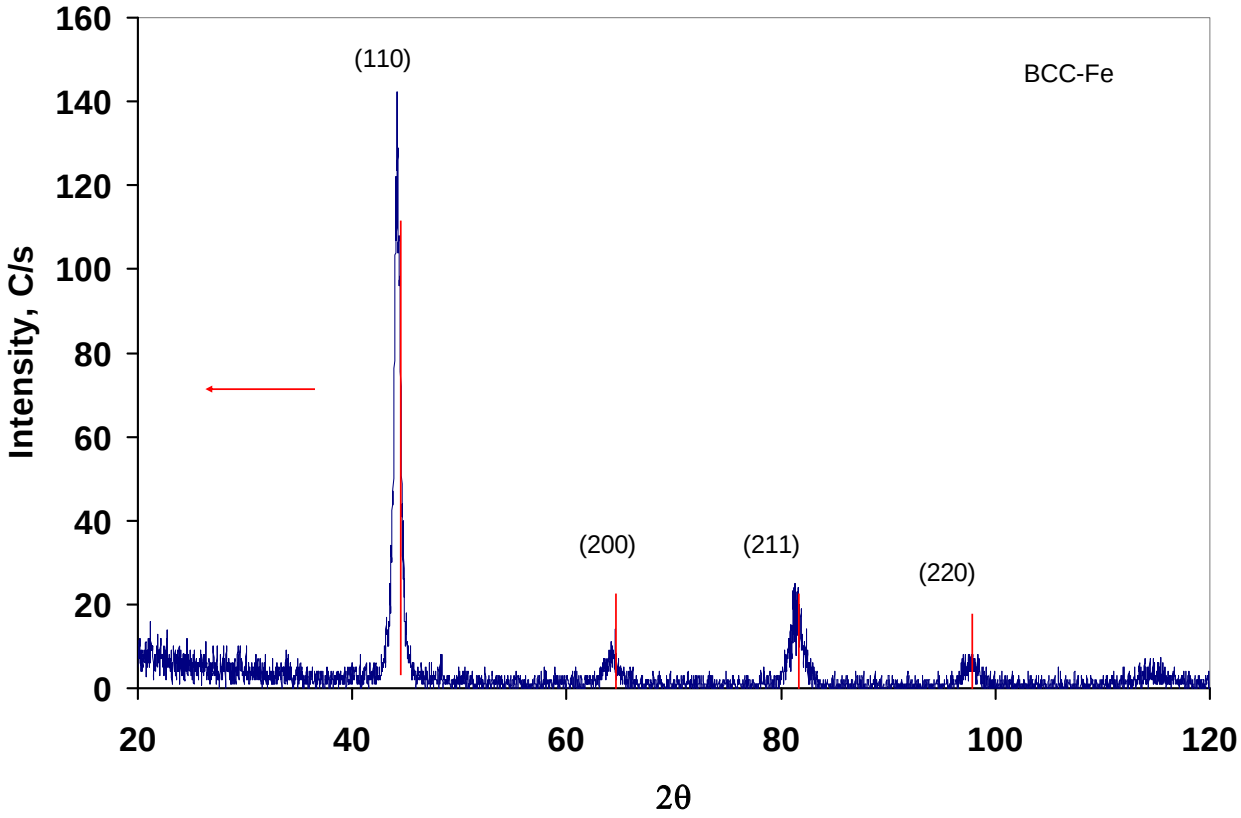

Fig. 3: XRD phase analysis of powder-1 deposit on SS316L. The image shows BCC-Fe peaks in the powder-1 deposit on SS316L substrate.

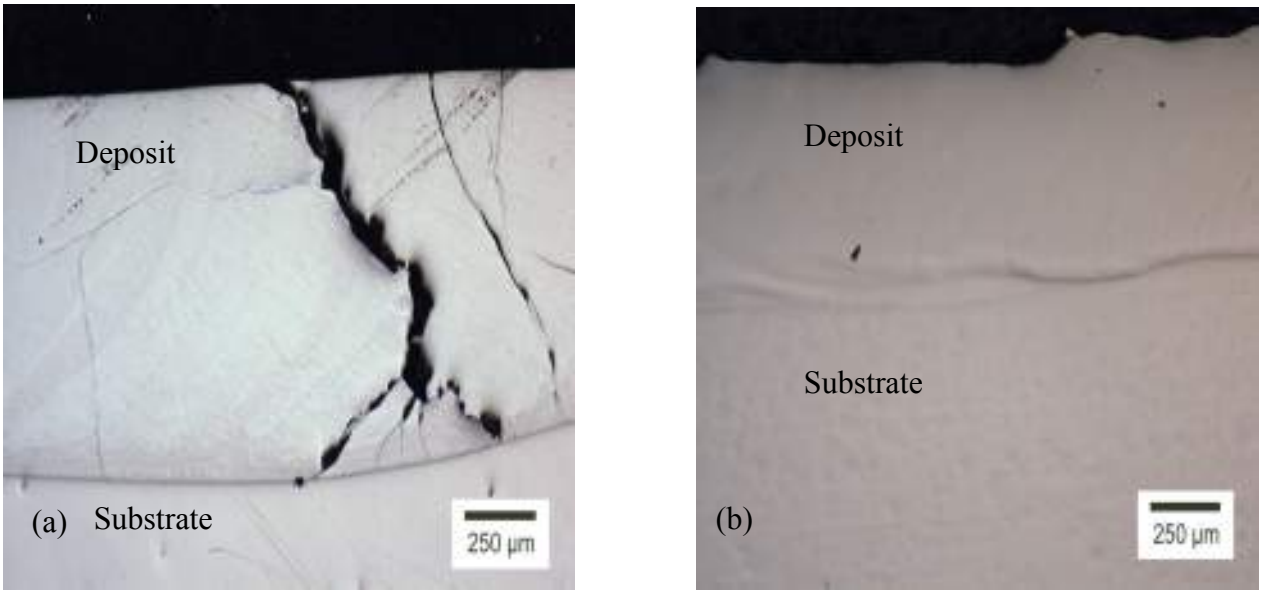

Fig. 4: Macrostructure of powder-2 deposit at 1000 W on (a) Ti6Al4V (shows macro-cracks); (b) SS316L (no macro-cracks) substrate.

Table 3: Composition analysis of powder-2 on Ti6Al4V and SS316L substrates for Ramp-up power profile *(wt % of V, Cr, Al, & Mo has not been reported in this table)

Exp. Type	Substrate	Power, W	Region	Reg. Type	Composition (wt%) Ti	Ni	Fe
Ramp-up	Ti64	300	1	Substrate	93.41		0.1
			2	Dilution	54.63	32.5	1.01
			3	Deposit	16.36	60.2	
		650	1	Substrate	92.37		0.26
			2	Dilution	59.2	29.6	0.92
			3		42.62	40	1.09
			4	Deposit	27.25	48	2.5
		1000	1	Substrate	93.47		0.26
			2	Dilution	58.59	27	0.77
			3		40.83	1.77	38.9
			4	Deposit	20.27	55.8	0.99
	SS316L	300	1	Substrate		7.38	73.9
			2	Dilution		39.4	36.1
			3	Deposit		67.5	3.48
		1000	1	Substrate		6.99	74.2
			2	Dilution		23.2	66.5
			3	Deposit		65.9	5.54

Figure 2b shows the equilibrium phase diagram of Ni-Ti alloy. The three most important IMPs in the phase diagram are Ti_2Ni, $TiNi_3$, and TiNi, which can contribute to cracking, while Ti-Cr and Ti-Mo form solid solutions over the entire composition range with no IMPs. Attempts to deposit powder-2 on Ti6Al4V substrate resulted in cracks due to residual stresses at all the processing parameters, while no cracks were observed when deposited on SS316L, an example shown in Fig. 4. A similar work carried out by Domack *et al* [14] showed macroscopic cracking in powder blends containing 40-60 percent Inconel 718 on Ti6Al4V substrate when produced by LMD. But Ni-based powders have been previously proven to bond well with steel in plasma-spraying, co-extrusion technique, or LMD [13,15] as there is no sigma/brittle phases present in the Fe-Ni equilibrium phase-diagram Fig. 2(c).

Table 4: Parameters for laser deposition of powder-1 on Ti6Al4V substrate

Laser Power, W	Travel Speed, ipm	Powder Feed Rate, g/min
455	20	3
535		
677		

X-map results for powder-2 on Ti6Al4V and SS316L substrate show self-grading in the melt pool for both the set of experiments, as an example shown in Fig. 5. Elements like Al (-substrate) and Cr (-deposit) did not diffuse into one another, whereas Mo is uniformly distributed in the melt pool. The composition data in Table 3 shows that the laser power does not play a very

significant role in controlling the inter-mixing in the melt pool. While that still holds true, laser power did result in segregation in the deposit. The deposit showed two discrete regions: (a) plume, and (b) non-plume. Plume- region consists of mixture of Ti+Ni, with higher weight percentage of Ti, while non-plume region has higher weight percentage of Ni. In general, Ni-Ti have relatively large negative enthalpy of mixing which results in the generation of additional heat in a very localized form in the melt pool, and hence aids the process of inter-mixing [16]. But segregation in the melt pool has shown that though inter-mixing was initiated, it remained incomplete during the deposition process at lower laser power levels. At higher powers, the dilution zone is wide with more inter-mixing. Also, enthalpy of mixing results in formation of a much localized heat source in the melt pool, and can either raise or lower its temperature. If rate of solidification is considered to be the temperature difference between melt pool and the surrounding substrate material. A higher temperature of the melt pool from exothermic mixing will result in higher solidification rate. Figure 6 shows composition data from EDS analysis plotted on the Ni-Ti equilibrium phase diagram: the plume –zone with higher wt% Ti falls in the lower melting point regions (obviously will solidify the last) compared to the non-plume zones. Also, the density of liquid Ti is very low compared to that of liquid Ni (twice that of liq. Ti) and therefore, the plume zone tries to move to the top along the solidification direction (Fig. 5). Because of the steeper slope of the liquidus NiTi line compared to that of Ti_2Ni, the driving force for NiTi formation will exceed that of Ti_2Ni. Therefore, NiTi will nucleate first (non-plume zone) from the liquid and Ti_2Ni will most likely form heterogeneously on it through peritectic reaction (plume zone) [17]. Since the composition data lies close to the TiNi and Ti_2Ni line compounds, it is safe enough to say that the possible cracking in the deposits is due to IMPs. In case of powder-2 on SS316L, we see only a small amount of Fe present in the deposit and no signs of cracks (Fig. 7 & Table 3). Because Fe-Ni are simple liquids with no interaction between them (Refer Phase Diagrams).

Table 5: Shows the composition data of powder-1 on Ti6Al4V substrate at different laser power levels

Laser Power	Composition wt% Ti	Fe	Al	V
677 W				
Substrate	89.45	0.18	6.82	3.55
Deposit-Bottom	36.51	12.83	3.72	46.95
Deposit-Middle	28.57	8.53	5.14	57.76
Deposit-Top	25.67	10.52	4.58	59.23
535 W				
Substrate	86.28	0.08	10.13	3.51
Deposit-Bottom	35.23	5.86	6.51	52.39
Deposit-Middle	20.24	8.49	5.07	66.2
Deposit-Top	13.67	9.3	4.4	72.63
455 W				
Substrate	88.66	0.35	7.32	3.66
Deposit-Bottom	27.63	11.07	3.62	57.66
Deposit-Middle	11.47	14.31	3.59	70.62
Deposit-Top	6.21	15.04	1.97	76.78

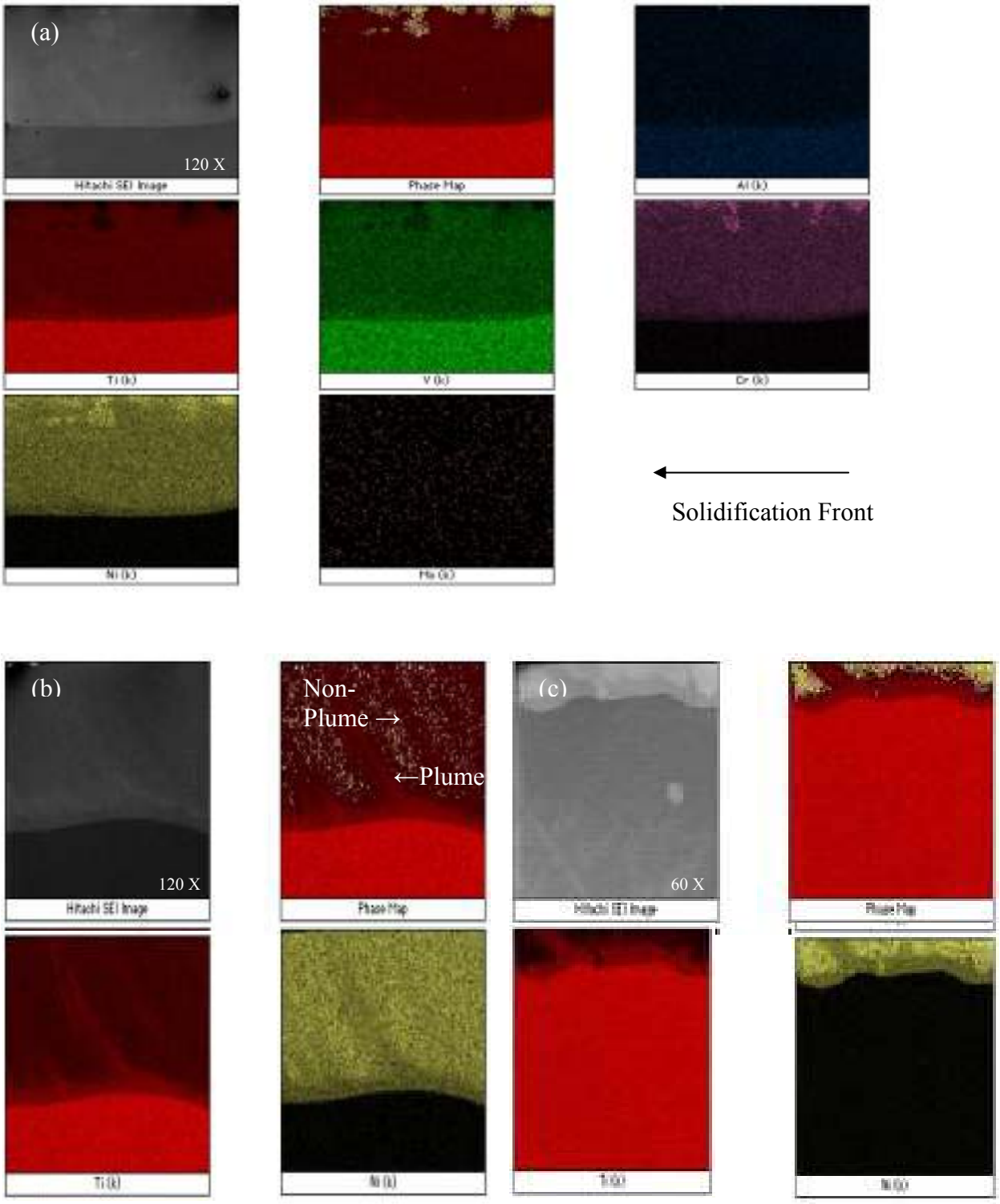

Fig.5: Shows X-mapping images of RAMP UP power profile of powder-2 on Ti6Al4V substrate at (a) 1000 W, (b) 600W, (c) 300 W. Due to incomplete inter-mixing, the melt pool is divided into plume and non-plume regions.

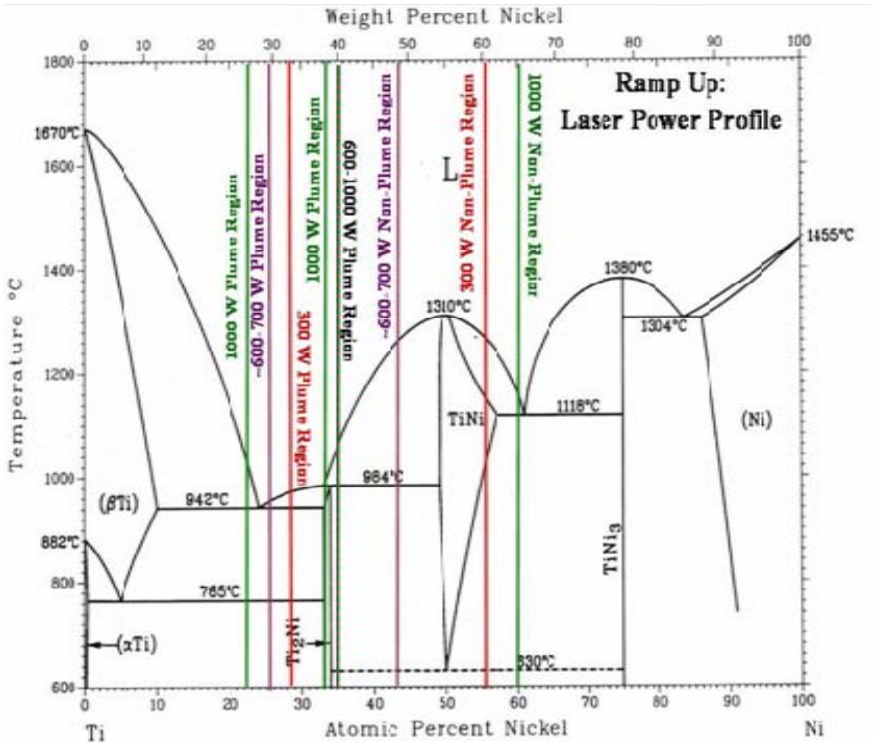

Fig. 6: Ni-Ti equilibrium phase diagram.

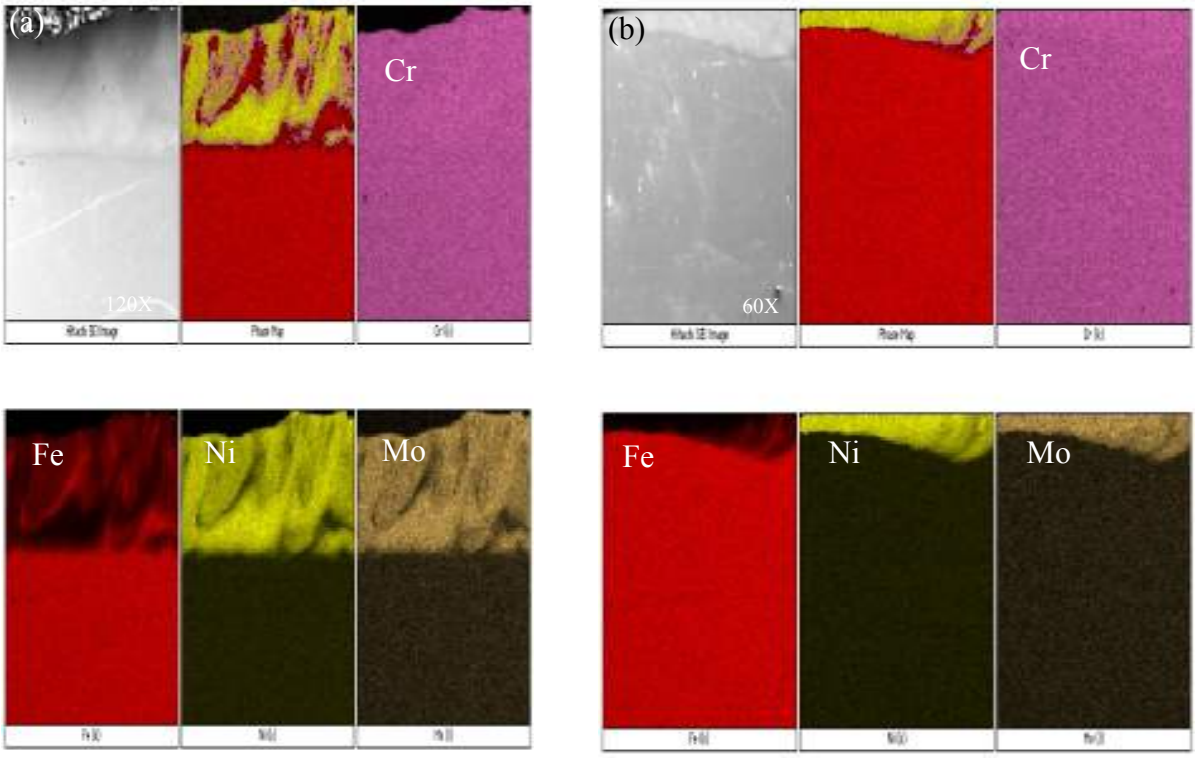

Fig. 7: Shows X-mapping images of RAMP UP power profile of powder-2 on SS316L at (a) 1000 W, and (b) 300 W. There is no inter-mixing in the melt pool.

A multi-layered deposition of powder-1 on Ti6Al4V substrate was performed to study the effect of laser power on intermixing/cracking. Table 4 lists the process parameters. The X- maps in Fig. 8 at 455 and 677 W show some amount of un-melted powder-1 particles at surface of the deposit. The composition analysis (Table 5) shows self-grading in the melt pool, although the four layers are not distinct. But all the deposits showed cracks either due to residual stresses or formation of IMPs. Ti-V forms good solid solution with no brittle phases, but Fe-xTi has two stable IMPs (FeTi and Fe_2Ti), and can contribute to brittle failure (Fig. 2(d)).

Table 6: Experimental parameters for deposition of powder-2 on Ti6Al4V substrate

Exp. No	**Power, W**	**Travel Speed, ipm**	**Powder Feed Rate, g/min**	**Pre-heating, ^oC**
1	300	10,20,30,40	5	540
2	600			
3	1000			

Table 7: Shows the composition data of powder-2 on Ti6Al4V substrate at different laser power levels *(wt % of V, Cr, Al, & Mo has not been reported in this table; shows composition for selected travel speeds; Composition of the substrate is Ti (92.57), V (3.95), Al (2.98); Sub□ Reg. 1 □ Reg. 2, etc.)

Power, W	**Trvl. Speed, ipm**	**Substrate heat, ^oC**	**Region**	**Ni**	**Ti**
300	10	nil	1	52.41	29.88
			2	48.85	37.35
			3	70.3	6.19
		540	1	20.65	70.49
			2	35.64	55.44
			3	44.94	42.53
			4	67.71	9.03
	20		1	23.65	68.29
			2	45.65	44.08
			3	52.82	29.85
			4	77.33	0.06
600	10	nil	1	24.35	66.85
			2	49.22	34.52
			3	48.85	35.38
			4	61.15	17.03
			5	63.04	14.98
			6	62.93	14.95
	20		1	26.85	60.08
			2	32.21	52.32
			3	32.16	52.18
			4	30.38	54.55
			5	30.48	54.32
	10	540	1	20.65	70.49
			2	35.64	55.44
			3	44.94	42.53

			4	67.71	9.03
	20		1	33.94	52.54
			2	40.45	41.84
			3	45.35	35.76
			4	46	35.15
			5	47.19	33.26
			6	47.68	32.58
1000	10	nil	1	24.67	64.75
			2	40.54	43.81
			3	46.82	36.01
			4	34.66	47.69
	20		1	26.85	60.03
			2	32.21	52.32
			3	32.16	52.18
			4	30.38	54.55
			5	30.48	54.32
	10	575	1	24.64	63.34
			2	40.87	42.53
			3	44.07	38.72
			4	43.4	39.39
			5	43.04	39.97
			6	43.04	39.71

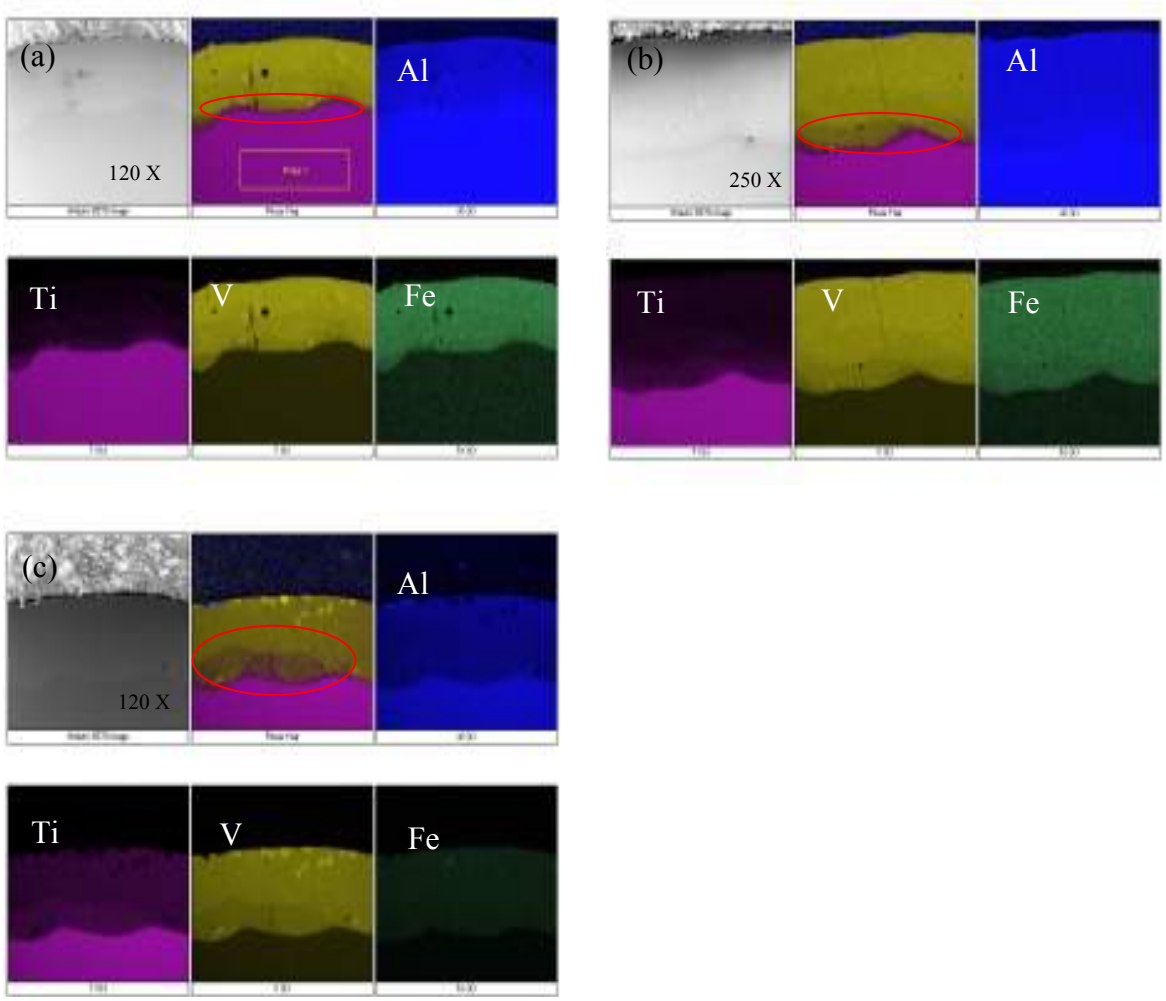

Fig. 8: Shows X-images of powder-1 on Ti6Al4V substrate at (a) 455 W, (b) 535 W, (c) 677 W. The four-layers are not distinguishable and cracks penetrated through the entire deposit.

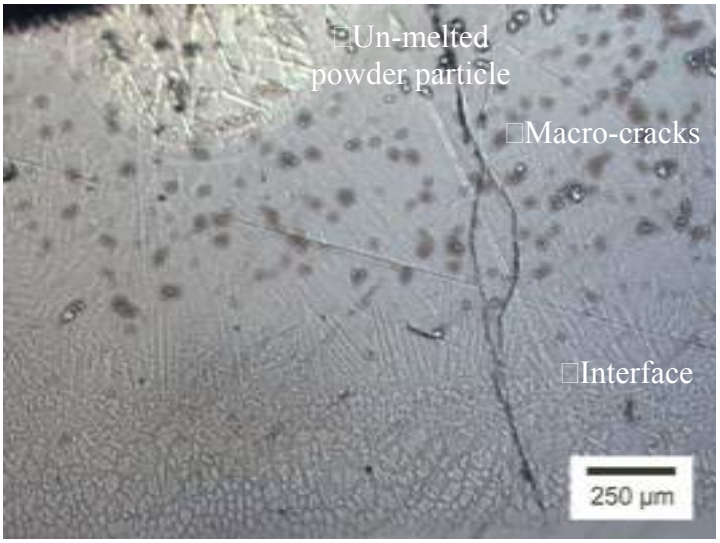

Fig. 9: Macro-cracks in powder-2 on Ti6Al4V substrate, 600 W, 10 ipm, substrate heating @ 540°C.

Inter-mixing and cracking in the layers for dissimilar materials are both inter-dependant problems. In order to obtain a defect free structure (cracks, pores, or bonding defects) the substrates were pre-heated to 540 °C on a hot plate and maintained at that temperature during the entire deposition process. Table 6 shows the process parameters of powder-2 deposit on (with/without pre-heat) Ti6Al4V substrates. The results show that a pre-heat temperature of 540°C is not sufficient enough to eliminate the cracks formed in the deposits, an example shown in Fig. 9. Kelbassa *et al* [18] showed that a pre-heating temperature between 650-700 °C was required to obtain a defect free single LMD tracks for γ-TiAl deposit on Ti6Al4V and γ-TiAl substrates. A suitable pre-heating guaranteeing a defect free LMD result is still under investigation. Also, the X-maps (Fig. 12) show that at 300 W for with/without substrate pre-heating there is significant amount of un-melted powder particles observed at the surface, and this was also true at 600 W without pre-heating for all the parameters. Though exothermic enthalpy of mixing does contribute additional heat to the melt pool, the melting efficiency is strongly affected by processing parameters and material thermo-physical properties [19]. A dimensionless-parameter model was previously used to estimate the melting efficiency for the LENS deposits. Equation [1] defines melting efficiency as ratio of energy required for melting ($A\Delta H_m$, per unit length) to actual absorbed energy ($\eta_a P/S$, per unit length).

$$\eta_m = Ch/Ry = SA\Delta H_m/\eta_a P \quad [1]$$
$$Ch = S^2A/\alpha^2$$
$$Ry = \eta_a PS/\alpha^2\Delta H_m$$

Where S is the heat-source travel speed, A is the total deposit cross-section, ΔH_m is the melting enthalpy, η_a is the laser energy efficiency (which is assumed to be 40 pct [19], α is the thermal diffusivity of the substrate [20], and P is the laser power. For materials with dissimilar thermo-physical properties [powder-2 (2.67 J/mm^3) onto Ti6Al4V (13 J/mm^3) substrate], an average value of melting enthalpy between the two was used, 7.8 J/mm^3 [19]. From the plot between *Ch* and *Ry* (Fig. 11(a)), melting efficiency can be determined solely from the dimensionless parameter *Ry*, for the material used in this study given by the following Equation [2]:

$$\eta_m = 0.1629 - (0.853/Ry) \quad [2]$$

At constant speed, the measured melting efficiency is slightly higher than that of the calculated value, Fig. 11(b). This discrepancy in the data can be attributed to the additional heat generated in the melt pool for dissimilar metals with exothermic enthalpy of mixing. The figure also shows how melting efficiency increases with the increase in the laser input power. It is previously reported that the calculated maximum melting efficiency for a moving point heat source in a 3D case is about 0.37 [20]. Also, Du pont *et al* [19] reported that increase in travel speed increases the melting efficiency as conduction can be neglected. In this case (Fig. 11(c)), the data contradicts the previously reported studies, which still need to be explained. Pre-heating the substrates to 540^{o}C before and during the deposition enhanced the inter-mixing in the melt pool for all the process parameters, as shown in Fig. 10. A significant amount of self-grading can be seen in the melt pool, as shown in Table 7. Geometric dilution '*D'* which is measured between the melted substrate and deposited powder is given by

$$D = A_s / (A_s + A_p) \quad [3]$$

Where A_s is the cross-sectional area of melted substrate and A_p is the cross-sectional area of deposited powder. The dilution increased with the increase in travel speed (Fig. 11(d)) as less power is delivered to the melt pool, resulting in decrease in deposit cross-sectional area. Also, dilution is affected by the melting efficiency. As the laser power is increased, more energy is available for melting the underlying substrate and incoming powder. Dilution was also observed to increase with substrate heating.

Microhardness

Hardness was measured along the samples (Fig. 12(a,b)) and through the samples (Fig. 12(c)). An average hardness value of 890±10 HV_{100} for powder-2 on Ti6Al4V substrate and 236±10 HV_{100} on SS316L substrate was obtained. A high hardness value in the former case may be due to the presence of brittle IMPs. The deposits were also tested at higher loads to study their performance. A small crack initiated in powder-2 on Ti6Al4V substrate at a load of 9.81 N (@ 5 s), while multiple cracks originated at 19.6N (@ 5 s). In case of powder-2 on SS316L, higher loads produced bigger indents indicating that the deposit is ductile/soft. Hardness as a function of depth for powder-1 on Ti6Al4V substrate at 1 N load, for 5 secs is shown in Fig. 12(c). The profile can be divided into three distinct regions: clad, dilution and heat affected zones (HAZ). The hardness of the dilution zone initially shown to increase and after which dropped to value equal to HAZ. Such a sharp transition in hardness values can be potential reasons for cracks either due to residual stresses or IMPs.

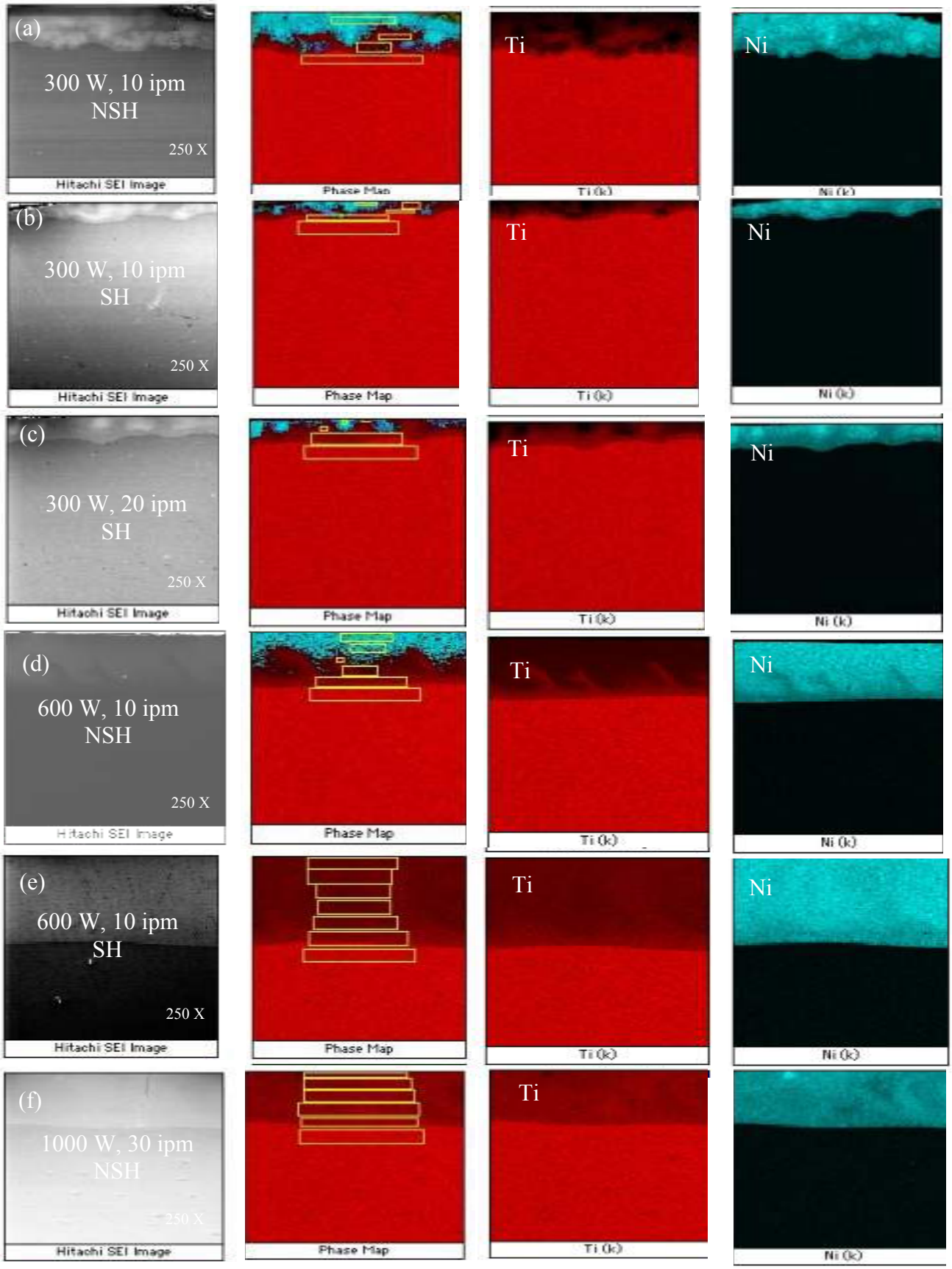
(a)
300 W, 10 ipm
NSH
250 X
Hitachi SEI Image
Phase Map
Ti
Ti (k)
Ni
Ni (k)
(b)
300 W, 10 ipm
SH
250 X
Hitachi SEI Image
Phase Map
Ti
Ti (k)
Ni
Ni (k)
(c)
300 W, 20 ipm
SH
250 X
Hitachi SEI Image
Phase Map
Ti
Ti (k)
Ni
Ni (k)
(d)
600 W, 10 ipm
NSH
250 X
Hitachi SEI Image
Phase Map
Ti
Ti (k)
Ni
Ni (k)
(e)
600 W, 10 ipm
SH
250 X
Hitachi SEI Image
Phase Map
Ti
Ti (k)
Ni
Ni (k)
(f)
1000 W, 30 ipm
NSH
250 X
Hitachi SEI Image
Phase Map
Ti
Ti (k)
Ni
Ni (k)

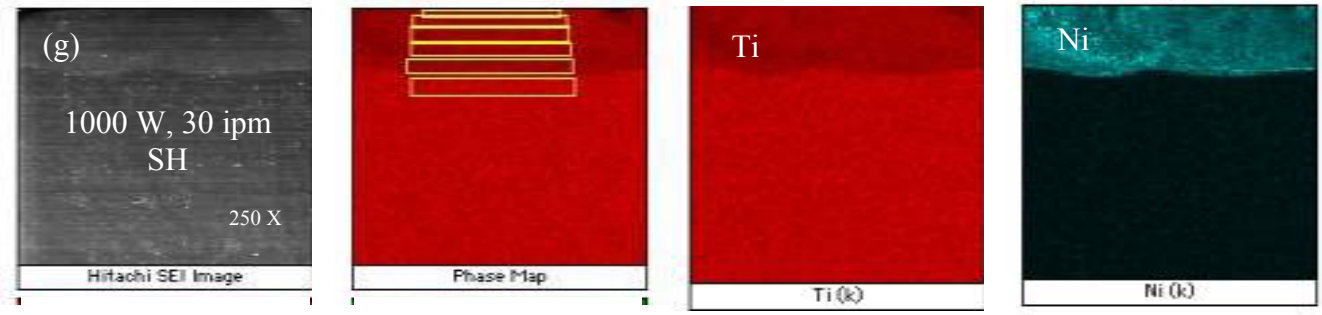

Fig. 10: X-maps of powder-2 deposit on Ti6Al4V substrate under different process parameters: SH = substrate heating, NSH = no substrate heating. Substrate heating increased the dilution zone size.

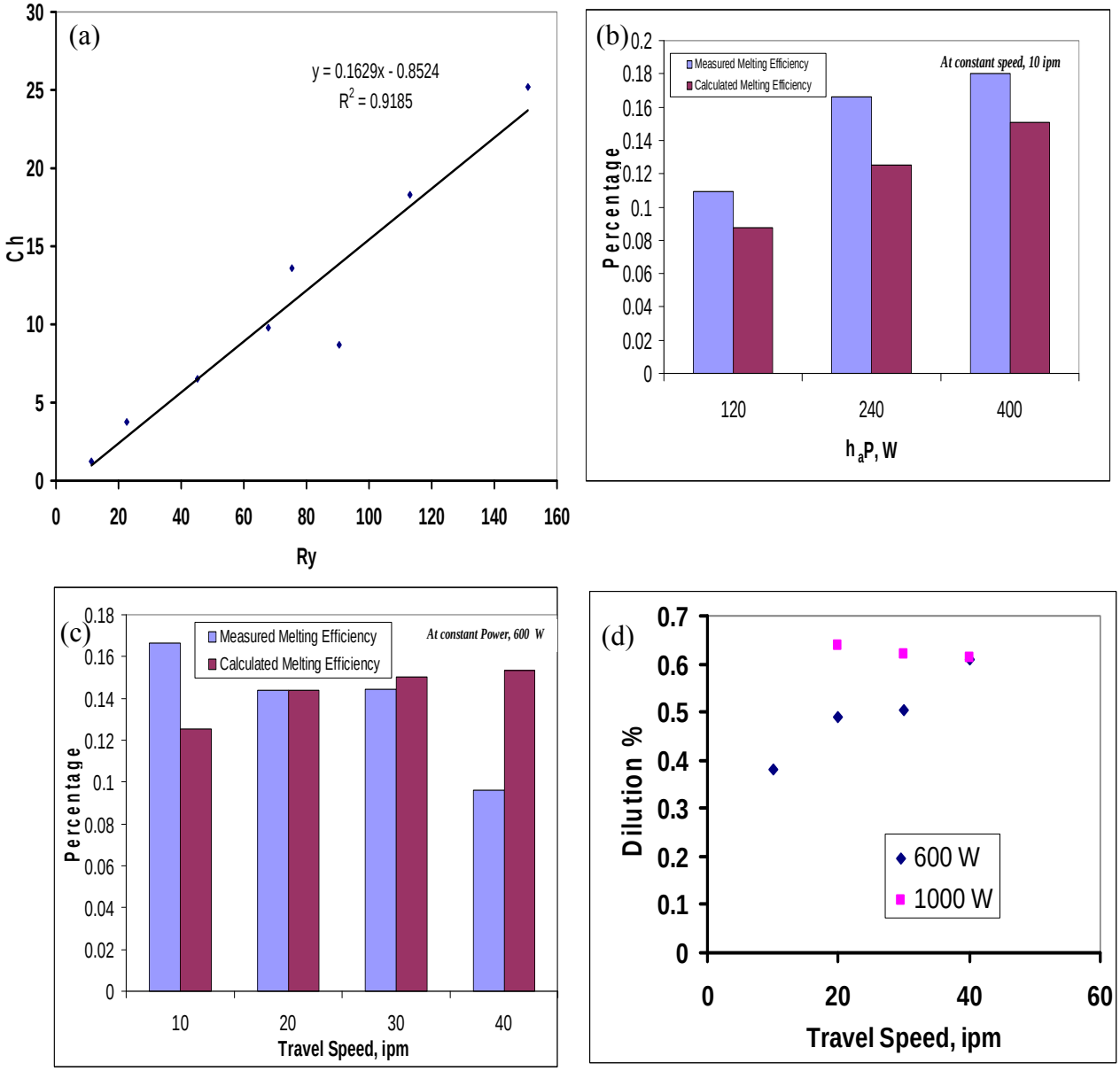

Fig. 11: (a) Plot between *Ch* Vs *Ry*; (b) melting efficiency at constant speed; (c) melting efficiency at constant power; (d) dilution.

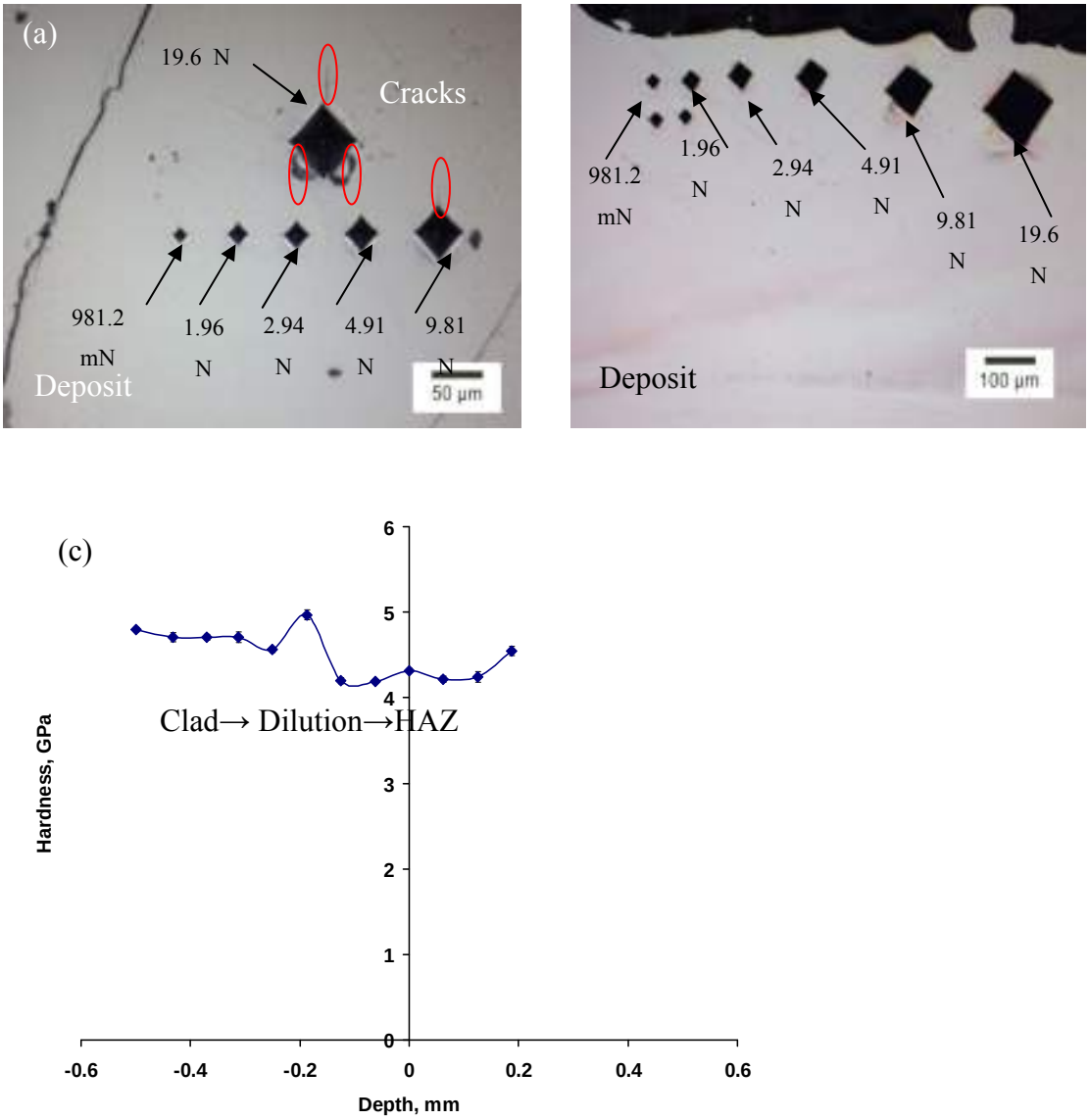

Fig. 12: Microhardness indents using different loads indicated for powder-2 on (a) Ti6Al4V, (b) SS316L substrates; (c) hardness as a function of depth for powder-1 on Ti6Al4V.

Summary

Inter-mixing and cracking are inter-related problems which need to be addressed while building FGMs with dissimilar materials. An optimized window of processing parameters like laser power, travel speed and powder feed rate is yet to be determined to obtain a successful FGM. Inconel-625 deposits showed macro-cracks due to combined effect of IMPs and residual stresses on Ti6Al4V substrates, while no cracks were observed on SS316L substrates. The possible IMPs present in the deposits were NiTi and $NiTi_2$. Intermixing and cracking was also observed on multi-layered (MLs) deposits of Fe-82wt%V on Ti6Al4V substrates. An attempt to counter the cracking issue in dissimilar materials by substrate treatment to 540^{o}C did not solve the problem either. Substrate heating prior and during the deposition enhanced inter-mixing in the melt-pool. The geometric dilution (D) increased with increase in laser power, travel speed

and substrate heating. Future work would involve optimization of parameters for these systems to reduce inter-mixing and cracking in the deposits, building MLs thin –walls and develop a simulation-model to study the melt-pool dynamics.

Acknowledgement

This research was supported by a grant from the U.S. Air Force Research Laboratory contract # FA8650-04-C-5704. Support from Missouri S&T Intelligent Systems Center is also greatly appreciated.

References

1. G. K. Lewis,U , E. Schlienger, Materials and Design, 21 (2000), p417.
2. S. M. Kelly, S. L. Kampe, Metallurgical and Materials Transaction A, 35A (2004), p1861.
3. P.A. Kobryn, E.H. Moore, S.L. Semiatin, Scripta Materialia, 43 (2000) p299.
4. G.P. Dinda , A.K. Dasgupta , J. Mazumder, Materials Science and Engineering A 509 (2009), p98.
5. M. Grenier, D. Dube, A. Adnot, M. Fiset, Wear, 210 (1997), p127.
6. V.M. Weerasinghe, D.R.F. West, J. de Damborenea, J. Material. Process.Technol., 58 (1996), p79.
7. X. Chen, G. Wu, R. Wang, W. Guo, J. Yang, S. Cao, Y. Wang, W. Han, Surf. Coat. Technol., 201 (2007), p4843.
8. L. Covelli, F. Pierdominici, I. Smurov, S. Tosto, Surf. Coat. Technol., 78 (1996), p196.
9. J.H. Abboud, R.D. Rawlings, D.R.F. West, Mater. Sci. Technol., 10 (1994), p414.
10. Y.T. Pei, V. Ocelik, J.Th.M. De Hosson, Acta Materialia, 50 (2002), p2035.
11. R.L. SunU, D.Z. Yang, L.X. Guo, S.L. Dong, Surf. Coat. Technol., 132 (2000), p251.
12. P.C. Collins, R. Banerjee, H.L. Fraser, Scripta Materialia, 48 (2003), p1445.
13. X. Lin, T.M. Yue, H.O. Yang**,** W.D. Huang**,** Acta Materialia, 54 (2006), p1901.
14. M S Domack, J M Baughman, Rapid Prototyping Journal, 11 (2005), p41.
15. F. J. Kahleen, A. V. Klitzing, A. Kar, J. of Laser Applications, 12 (2000), p205
16. K. I. Schwendner, R. Banerjee, P. C. Collins, C. A. Brice, H. L. Fraser, Scripta Materialia, 45 (2001), p1123.
17. S. Chatterjee, T.A. Abinandanan, K. Chattopadhyay, J. of Materials Science, 41 (2006), p643.
18. I. Kelbassa, A. Welsheit, K. Wissenbach, V. Hermes, Proc. of the 2nd Pacific International Conference on Applications of Lasers and Optics, 2006, p208.
19. R. R. Unocic, J. N. Du. Pont, Metallurgical and Materials Transactions B, 34B (2003), p439.
20. M. Van Elsen, M. Baelmans, P. Mercelis, J. P. Kruth, International Journal of Heat and Mass Transfer, 50 (2007), p 4872.